Journal of Materials Chemistry C

ROYAL SOCIETY OF CHEMISTRY

PAPER

View Article Online
View Journal | View Issue

Cite this: J. Mater. Chem. C, 2025, 13, 18712

A-site cation modification of Cs-based perovskite thin film for green light-emitting diodes

Ethan H. Jansen,[a] Benjamin York,[a] Souk Y. Kim,[b] Jeffrey Shallenberger,[c] Ivy M. Asuo,[bc] Nutifafa Y. Doumon *[bcd] and Kester O. Ighodalo *[a]

Received 16th March 2025,
Accepted 8th August 2025

DOI: 10.1039/d5tc01143d

rsc.li/materials-c

Light-emitting diodes based on metal halide perovskites have gained significant research interest due to their exceptional properties, including tunable emission wavelengths and high photoluminescence quantum yield (PLQY), and offer the potential for solution-based fabrication. However, the antisolvent approach in forming perovskite thin films and the delicate modification of A-site cations in metal halide perovskite materials remain ongoing topics of discussion. In this study, we investigate the morphology, crystal structure, photoluminescence, and optical and photoelectronic spectroscopy characteristics of perovskite materials containing cesium (Cs^+) and a mixture of formamidinium (FA^+) and Cs^+. We begin by exploring the formation of $CsPbBr_3$ perovskite films using three different antisolvents, including chlorobenzene (CB) and eco-friendly solvents toluene and anisole. Our findings indicate that toluene significantly improves the surface morphology and crystallinity of the film compared to anisole and CB, and a small portion of FA^+ in Cs-based perovskite potentially influences charge transport in device applications. Based on these results, we use toluene for $FA_xCs_{1-x}PbBr_3$ ($0 < x < 0.15$) perovskite thin films for the rest of the study. The results show that incorporating a small portion of FA^+ in Cs-based perovskite, annealed at different temperatures, leads to enhanced crystallinity, larger grain sizes, a negligible change in the band gap, effective charge transport, and improved device luminance. These findings broaden the A-site cation options for efficient mixed-cation perovskite light-emitting diodes.

Introduction

Metal halide perovskite light-emitting diodes (PeLEDs) have gained significant attention in recent years, achieving external quantum efficiencies (EQE) of above 25%. This is largely due to ongoing research efforts in different deposition techniques and dimensionality engineering, including composition, interfacial modifications, anti-solvent, and various additives in perovskite light-emitting layers.[1–4] Moreover, outstanding features such as tunable emission color, easy solution processing, high absorption coefficient, excellent carrier mobility, and charge transport make perovskite materials promising candidates for solid-state lighting technologies and next-generation displays.[5–7] The 3D framework of perovskites generally adopts the chemical formula ABX_3, where A is a monovalent cation such as methylammonium (MA^+), formamidinium (FA^+), cesium (Cs^+), potassium (K^+), as well as other alternatives, which include phenethylamine (PEA), as well as polymeric ammonium cations like polyethyleneimine (PEI). B is a divalent cation, which is mostly lead (Pb^{2+}) or tin (Sn^{2+}), while X is an anion and is typically a halide such as iodide (I^-, Br^-, and Cl^-).[8–10] Due to the Goldschmidt tolerance factor, only certain cations, such as FA^+, Cs^+, and MA^+, with ionic radii of 2.79 Å, 1.81 Å, and 2.70 Å, respectively, can be used in the 3D perovskite crystal structure.[11,12]

Many properties of 3D perovskite, such as the band gap, crystal stability, and optical properties, depend on the choice of antisolvents, but are highly dependent on the nature of the A-site cations. These cations have been widely utilized in PeLEDs to enhance their optoelectronic properties, including improved electroluminescence (EL) performance, photoluminescence quantum yield (PLQY), and external quantum efficiency, as well as extended operational lifetime.[13–15] Most high-performance PeLEDs are FA^+-based perovskites since the MA^+-based perovskites suffer from poor stability at higher temperatures, affecting long-term optoelectronic properties and hindering future applications.[16] Thus, Cs^+ have been introduced to enhance the MA^+-based perovskite systems.[17–19] For example, incorporating Cs^+ into $MAPbBr_3$ has been shown to possess superior surface morphology and PLQY compared to $MAPbBr_3$ and a breakthrough

[a] Department of Physics, Hope College, Holland, Michigan, 49423, USA. E-mail: ighodalo@hope.edu
[b] Department of Materials Science and Engineering, The Pennsylvania State University, University Park, PA, 16802, USA. E-mail: nzd5349@psu.edu
[c] Materials Research Institute, The Pennsylvania State University, University Park, PA, 16802, USA
[d] Department of Engineering Science and Mechanics, The Pennsylvania State University, University Park, PA, 16802, USA

in the luminescence of 24 500 cd m^{-2}, nearly tenfold higher, was achieved through Cs^+ doped $MAPbBr_3$ green-light emitting layer compared to $MAPbBr_3$.[13] This can be attributed to the optimized optoelectronic properties after composition modification, especially charge transport. Additionally, large-group ammonium bromide incorporation into the MA^+ cation system has also been explored.[6]

Recent studies indicate that incorporating inorganic Cs^+ into $FAPbBr_3$ improves film morphology and enhances optoelectronic properties.[20,21] For instance, Cho *et al.* demonstrated that adding Cs^+ to $FAPbBr_3$ significantly reduces both the average grain size and trap density, thereby effectively improving charge transport. As a result, this modification leads to increased photoluminescence quantum efficiency (PLQE), prolonged PL lifetime, and improved current efficiency.[21] Furthermore, the exchange of MA^+, Cs^+, or FA^+ has been utilized to enhance thermal stability and modify the bandgap.[17,22] Many combinations of suitable A-cation combinations are employed in the fabrication of PeLED devices, employing various device structural configurations to optimize performance.[10,23–25] In addition, the FA^+ content modulation in Cs-based perovskites has been mostly explored, particularly in single crystals, nanostructures, and microplates;[26–28] thus, further in-depth studies in thin films are still needed. To enhance our understanding, we conducted a systematic analysis of FA^+ in $CsPbBr_3$ perovskite thin films, emphasizing the fabrication process, structural properties, and other relevant characteristics. By highlighting the significant progress in PeLEDs, we judiciously submit that there is room for further insight into the study of these components and their composition ratios.

In this study, we explored the formation of $CsPbBr_3$ perovskite films using three different antisolvents and the incorporation of a small portion of FA^+ into $CsPbBr_3$ perovskite with varied compositions, resulting in mixed-cation $FA_xCs_{1-x}PbBr_3$ ($0 < x < 0.15$) perovskite. We conducted a constructive investigation into the morphology, crystal structure, photoluminescence (PL) characteristics, and X-ray photoelectron spectroscopy (XPS) of the mixed-cation perovskite-emitting layer. We used the anti-solvent method[29–33] during spin-coating to assist the crystallization of the perovskite thin films, followed by annealing. In our experiments with various anti-solvents, we identified toluene as the optimal choice, as it produced superior quality thin film morphology and PL compared to anisole and chlorobenzene (CB). After annealing the toluene-processed mixed-cation perovskite thin films at different temperatures, we observed that increasing the ratio of FA^+ effectively induced a redshift in the PL emission wavelength. Further enhancement in this effect is noticed in thin films subjected to high-temperature annealing. Our findings indicate that higher FA^+ ratios and elevated temperatures contribute to larger grain sizes and increased film roughness, alongside shifts in the X-ray diffraction (XRD) peaks towards higher angles. This structural modification plays a crucial role in influencing electronic properties, including bandgap and

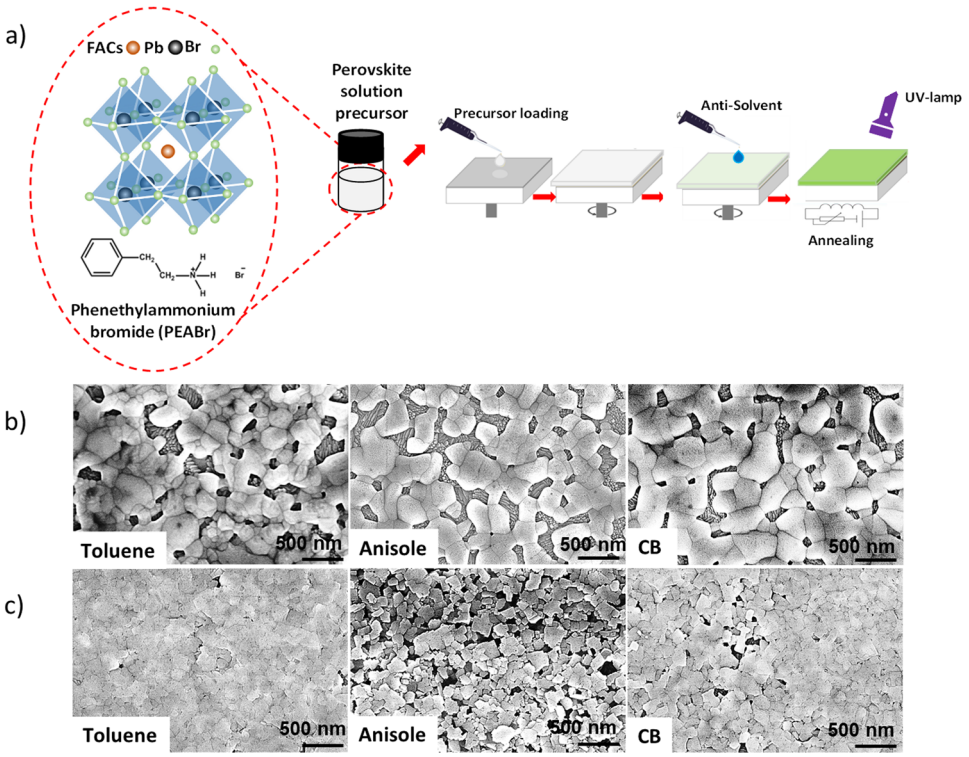

Fig. 1 Fabrication process and morphological characterization of $CsPbBr_3$ perovskite films. (a) Schematic of the chemical structures and facile solution-based fabrication procedure of the perovskite film with PEABr additive. SEM image of (b) pristine $CsPbBr_3$ films and (c) $CsPbBr_3$:PEABr films with toluene, anisole, and CB.

charge carrier transport. To understand the mechanism, it is essential to note that FA^+, which is partially substituted, can lead to a significant increase in Br^- concentration and a slight increase in the lattice structure, resulting in a peak luminance higher than that of Cs-based films, as indicated by our preliminary results. Our work closes the gap and provides new insights into A-site cation engineering in Cs-based perovskite emitting layers, which can be significant for advancing PeLEDs.

Results and discussions

We fabricated perovskite thin films through a one-step spin-coating process using perovskite precursor solutions, as described in the experimental section. Fig. 1(a) depicts the chemical structures and casting process of the solution-based layer. To attain the best quality perovskite thin films, optimized surface morphology and control of the crystallization and growth are imperative. This is particularly crucial due to the observed low surface coverage and poor film morphology of pristine Pb-based perovskite films. The presence of pinholes in the perovskite films can significantly increase non-radiative recombination and impede charge transport within the perovskite layer, thereby affecting the overall properties and performance.[8,34,35]

Reports suggest that high molar excess ratios of PEABr may cause blue wavelength emission, leading to the formation of a 2D perovskite film with varying absorption peaks.[36] This was also confirmed in the absorbance and PL measurement (Fig. S1). Based on this, for optimization, we added a 40% molar excess ratio of PEABr solution to the $CsPbBr_3$ perovskite solution to improve the film morphology. Next, we investigated the impact of anti-solvent treatment on the morphological and optical properties of the film before fabricating the $FA_xCs_{1-x}PbBr_3$ ($0 < x < 0.15$) perovskite films. Fig. 1(b and c) displays the SEM images of three distinct perovskite thin films on glass/ITO treated with toluene, anisole, and CB before and after optimization, respectively. Before optimization, as shown in Fig. 1(b), all perovskite films treated with toluene, anisole, and CB exhibited poor film coverage and pinholes with huge gaps in various areas of the SEM image. After optimization, we observed that the perovskite thin films treated with toluene exhibited a slightly different morphology compared to the best compact films, as shown in Fig. 1(c), which were treated with CB and anisole, respectively. The toluene-based thin films show better surface coverage with fewer pinholes and almost no gaps in various areas of the SEM image, as shown in Fig. 1(c).

We conducted AFM measurements on the perovskite films, as shown in Fig. S2, and found that the average roughness of the thin films treated with toluene (2.1 nm) is less than that of the films treated with CB (3.2 nm) and anisole (4.5 nm). We also investigated the effects of the different anti-solvent treatments on the optical properties of the optimized perovskite films. Fig. (2a and b) shows the absorption and photoluminescence (PL) spectra of optimized $CsPbBr_3$ films treated with toluene, anisole, and CB.

Fig. 2(a) shows similar absorption spectra of perovskite films treated with toluene, anisole, and CB, with the optical bandgap exhibiting a small change, *i.e.*, 2.37 eV for toluene, and 2.42 eV and 2.41 eV for anisole and CB, respectively. As shown in Fig. 2(b), we observed a slight peak shift towards higher wavelengths (redshift) for the perovskite thin film treated with toluene and an intense PL intensity, indicating that toluene exposure helps form a higher quality film. Thus, the morphology and PL characteristics of the perovskite film treated with toluene point to better performance than those treated with anisole and CB.

For the rest of the study, we fabricated the $FA_xCs_{1-x}PbBr_3$ ($0 < x < 0.15$) perovskite film using toluene as the antisolvent. We added different molar excess ratios of the PEABr solution (0% to 100%) to the $FA_xCs_{1-x}PbBr_3$ ($0 < x < 0.15$) precursor solution and annealed the thin films at different temperatures. A detailed description of the procedure, from perovskite solution preparation to film fabrication steps, is provided in the experimental section. Fig. S3–S6 show the images of $FA_xCs_{1-x}PbBr_3$ ($0 < x < 0.15$) of the fabricated perovskite thin films under UV light. We observed that the brightness of the

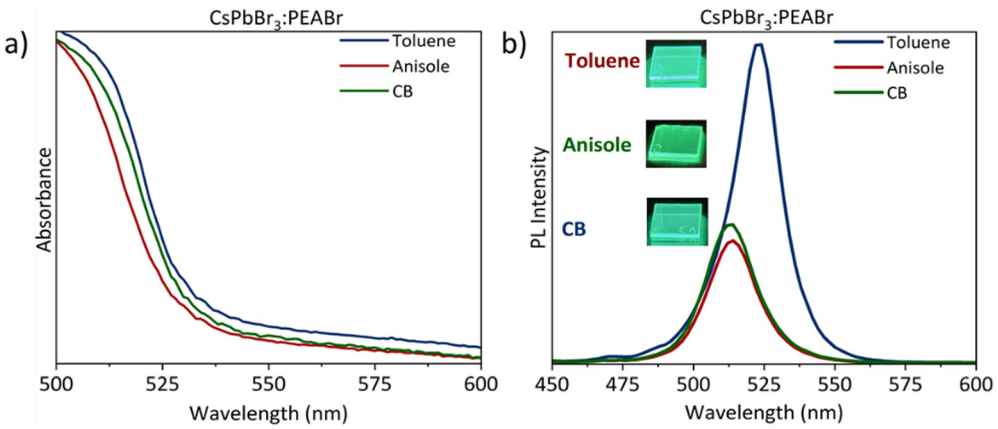

Fig. 2 Optical characterization of optimized $CsPbBr_3$ perovskite films. (a) Absorbance and (b) PL spectra measurements of $CsPbBr_3$:PEABr films treated with toluene, anisole, and CB.

various perovskite films tends to increase when the FA^+ ratio and annealing temperature are increased (Fig. S3–S6). We chose a 40% molar excess ratio of PEABr to gain a clearer understanding of the impact of incorporating FA^+ into $CsPbBr_3$ perovskite and the effect of higher annealing temperatures on the optical, morphological, photoelectrical, and structural properties of the films. The 40% molar excess ratio of PEABr is optimum for the green emission in the thin films and also at the borderline between green and blue emissions, considering all our studied perovskite thin films.

To elucidate the optical properties, we conducted absorption and PL measurements on thin films deposited onto glass substrates. Fig. 3(a–d) shows absorption and PL spectra of optimized $FA_xCs_{1-x}PbBr_3$ ($0 < x < 0.15$) films annealed at different temperatures (70 °C, 90 °C, and 110 °C). Fig. 3(a) shows the absorption spectra for $FA_xCs_{1-x}PbBr_3$ ($0 < x < 0.15$) perovskite films. As shown in Fig. (3a), we observed slight redshifts towards the higher wavelength as the annealing temperature increased. Furthermore, as the FA^+ increases, the absorption edge slightly shifts toward higher wavelengths, as shown in Fig. S7, due to orbital overlap.[37] The optical bandgap showed a variation between 2.37 eV and 2.44 eV with the various treatments, as shown in Table S1. Therefore, incorporating FA^+ into $CsPbBr_3$ perovskite and different annealing temperatures affects the absorption of the perovskite thin films. The redshift in the absorption edge was also observed in the PL spectra, as shown in Fig. 3(b). Compared with pure Cs films, no significant peak shift occurred with smaller FA^+ ratio films annealed at low annealing temperatures. With a further increase of FA^+ ratio and annealing temperature, noticeable changes in peak shifts toward higher wavelengths were observed in $FA_{0.05}Cs_{0.9}$-110, $FA_{0.10}Cs_{0.90}$-110, and $FA_{0.15}Cs_{0.85}$-110 films, as seen in Fig. 3(b).

We plotted the PL intensities of $FA_xCs_{1-x}PbBr_3$ ($0 < x < 0.15$) films annealed at 70 °C as illustrated in Fig. 3(c) to further demonstrate the effect of incorporating PEABr and FA^+. The PL intensity for the $FA_{0.05}Cs_{0.95}$-70 °C film showed a higher PL intensity (Fig. 3(c)) as compared to pure Cs-70 films due to the presence of defects and traps in the pure Cs films. The higher PL intensity indicates an effective recombination of charge carriers, which can be attributed to the improved charge transport.[38,39] This suggests that incorporating FA^+ into the films can positively influence charge transport in the perovskite active layer. The presence of defects and traps in the perovskite active layer is known to influence the charge transport mechanism in the device. Therefore, time-resolved photoluminescence (TRPL) measurements were carried out to investigate the charge carrier dynamics in the perovskite thin films deposited on glass substrates. The carrier lifetimes were obtained from a biexponential fitting of the TRPL spectra and presented

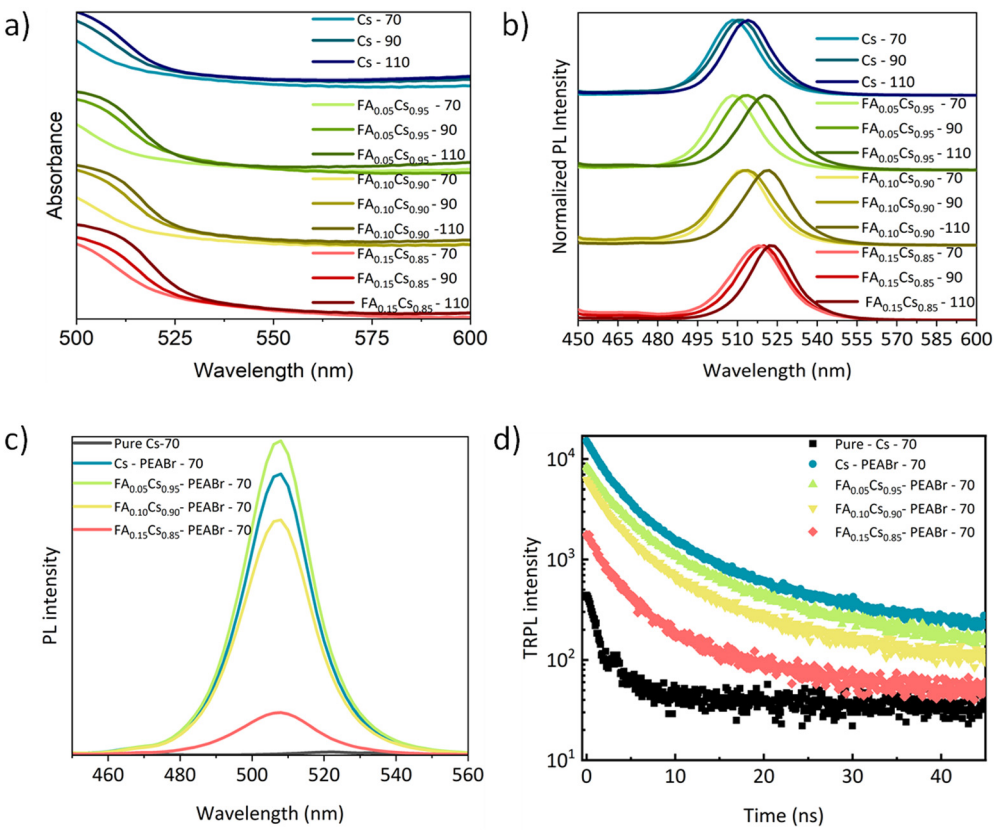

Fig. 3 Optical characteristics of $FA_xCs_{1-x}PbBr_3$ ($0 < x < 0.15$) perovskite films. (a) Normalized absorbance measurement at different temperatures (70 °C, 90 °C, and 110 °C) and (b) normalized PL spectra at different temperatures (70 °C, 90 °C, and 110 °C). Selected (c) PL spectra and (d) TRPL spectra of films at 70 °C.

in Fig. 3(d). Generally, the shorter or faster lifetime, τ_1, is linked to bulk recombination of the trapped charges, and the slower decay or longer time, τ_2, is related to the radiative recombination of the charge carriers in the material.[31,40] In comparison to the lifetimes of the pure Cs-70-based films, the lifetimes increased upon the incorporation of the FA^+ and PEABr additives. Both the time constants increased from τ_1 = 0.95 ns and τ_2 = 5.66 ns for Cs-70 to τ_1 = 2.42 ns and τ_2 = 8.78 ns for $FA_{0.05}Cs_{0.95}$-70, respectively (Table S2). A slight difference in the time constants was also observed for other FA^+ ratios. This evidence suggests that the FA^+ and PEABr additives improve the interfacial charge transfer, resulting in suppressed non-radiative recombination. This suppression could enhance the carrier lifetimes and device performance, potentially leading to more efficient perovskite light-emitting diodes.

We selected Cs-70, $FA_{0.05}Cs_{0.95}$-70, $FA_{0.10}Cs_{0.90}$-70, $FA_{0.15}Cs_{0.85}$-70, $FA_{0.05}Cs_{0.95}$-110, and $FA_{0.15}Cs_{0.85}$-110 films, as illustrated in Fig. S8, to probe further the effect of incorporating FA^+ and annealing temperatures. Fig. 4(a–f) displays the SEM images of six selected perovskite thin films on glass/ITO. From the SEM images, as shown in Fig. 4(a–d), the grain size of the perovskite film with $FA_{0.15}Cs_{0.85}$-70 is enlarged compared to the perovskite film with Cs-70. Also, with an increase in the annealing temperature, we found that the grain size of $FA_{0.05}Cs_{0.95}$-110 films and $FA_{0.15}Cs_{0.85}$-110 films (Fig. 4(e and f)) enlarged compared to $FA_{0.05}Cs_{0.95}$-70 and $FA_{0.15}Cs_{0.85}$-70, as shown in Fig. 4(b and d). Previous work reported that enlarged grain sizes facilitate charge carrier transport and enhance carrier mobility within the perovskite films. This improvement occurs because these characteristics help reduce pinholes, grain boundaries, and defect density at the grain boundaries.[7,41,42] The enlarged grain size can effectively contribute to the high PL intensity, as shown in Fig. 3(c).

To further validate the effect of FA^+ and annealing temperature and the enlarged grain size observed in our SEM images, we conducted AFM characterization. Fig. 5(a–f) shows the surface morphology and roughness of six selected perovskite thin films on glass/ITO. As shown in Fig. 5(a), the perovskite film roughness for Cs-70 shows a roughness value of 2.7 nm. With the increase in the FA^+ ratio, the roughness increased to 5.9 nm for the $FA_{0.15}Cs_{0.85}$-70 perovskite film. An increase in the annealing temperature increased the film roughness of $FA_{0.05}Cs_{0.95}$-110 films and $FA_{0.15}Cs_{0.85}$-110 films to 3.8 nm and 6.8 nm, respectively (Fig. 5(e and f)), with the enlarged grain size more evident for $FA_{0.15}Cs_{0.85}$-110 films, as shown in Fig. 5(f).

Fig. 6(a–d) displays the XRD pattern of the six selected perovskite thin films on glass/ITO shown in Fig. S8. All XRD patterns are characterized by a peak positioned at $2\theta \approx 15.2^\circ$ and 30.6°, indicating the formation of (100) and (200) crystal planes.[43] The perovskite films exhibited a cubic crystalline structure with a diffraction peak at $2\theta \approx 15.18^\circ$ and a more intense diffraction peak at a known angle of 30.56°, as shown in Fig. 6(a and c). The magnified diffraction peaks in Fig. 6(b) show that the peaks at (200) shifted slightly toward a higher diffraction angle with an increased FA^+ ratio in Cs-based perovskite films. This shift can be attributed to the smaller Cs^+ ions being partially substituted by the larger FA^+ ions in the perovskite crystal structure, which reduces the interplanar crystal spacing. A shift towards higher angles was also observed at a higher temperature, as shown in the magnified diffraction peaks (Fig. 6(d)). These peaks confirm the successful formation of a highly crystalline perovskite structure. We also measured the average crystallite size using the (100) and (200) reflections of the selected perovskite thin films using Scherrer's eqn (1).

$$D = \frac{K\lambda}{B\cos\theta} \quad (1)$$

Here, K represents the Scherrer constant, which we assume to be 0.9, D is the crystallite size, B denotes the full width at half maximum (FWHM) of the measured diffraction peak, θ represents the diffraction angle, and λ stands for the X-ray wavelength (0.154 nm). Table S3 shows the crystallite size derived from the FWHM and Scherrer's equation of the perovskite films. The calculated crystallite sizes for the perovskite films Cs-70, $FA_{0.05}Cs_{0.95}$-70, and $FA_{0.10}Cs_{0.90}$-70 are 17.9 nm, 18.1 nm, and 18.7 nm, respectively. In contrast, the size for $FA_{0.15}Cs_{0.85}$-70 and $FA_{0.15}Cs_{0.85}$-110 decreases to 16.8 nm and 15.5 nm, respectively. Additionally, our results indicate that as the

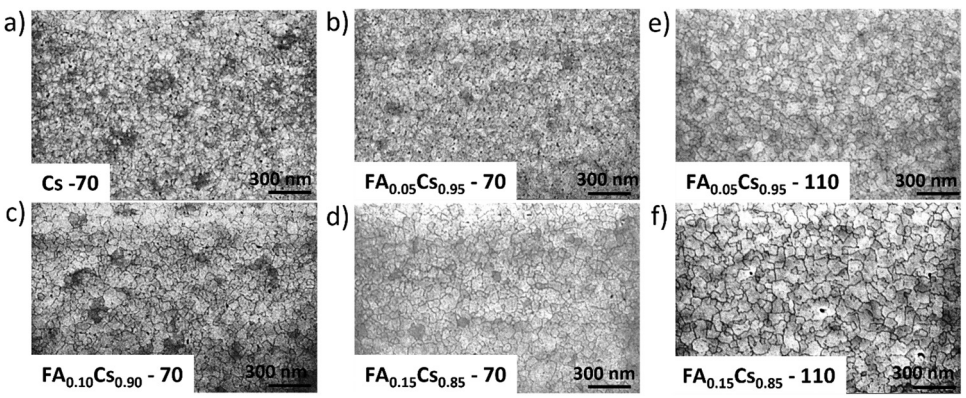

Fig. 4 Microstructure morphological characterization of $FA_xCs_{1-x}PbBr_3$ ($0 < x < 0.15$) perovskite films. SEM image for (a) $CsPbBr_3$, (b) $FA_{0.05}Cs_{0.95}PbBr_3$, (c) $FA_{0.10}Cs_{0.90}PbBr_3$ and (d) $FA_{0.15}Cs_{0.85}PbBr_3$ annealed at 70 °C, (e) $FA_{0.05}Cs_{0.95}PbBr_3$ and (f) $FA_{0.15}Cs_{0.85}PbBr_3$ annealed at 110 °C.

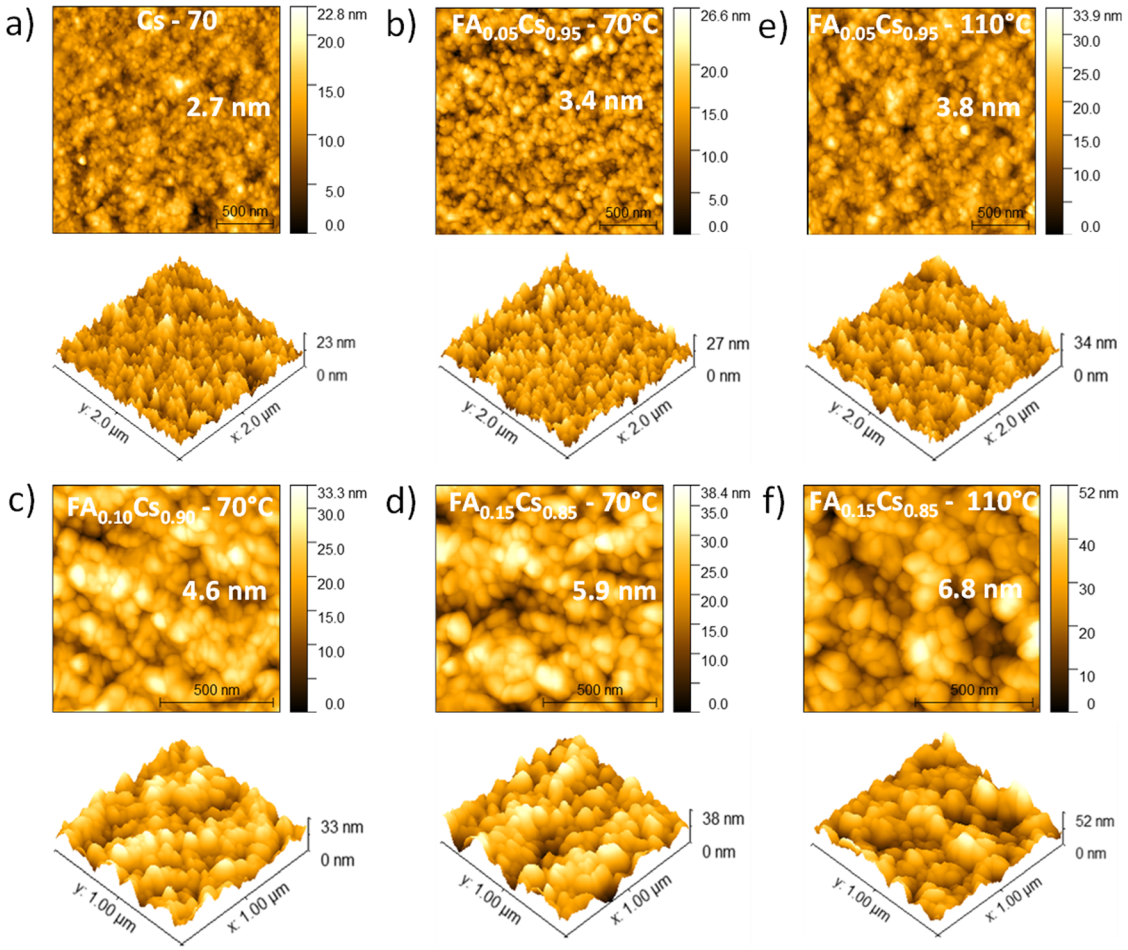

Fig. 5 Morphological characterization of $FA_xCs_{1-x}PbBr_3$ ($0 < x < 0.15$) perovskite thin films. AFM images of films annealed at 70 °C for (a) $CsPbBr_3$, (b) $FA_{0.05}Cs_{0.95}PbBr_3$, (c) $FA_{0.10}Cs_{0.90}PbBr_3$, and (d) $FA_{0.15}Cs_{0.85}PbBr_3$; and films annealed at 110 °C for (e) $FA_{0.05}Cs_{0.95}PbBr_3$ and (f) $FA_{0.15}Cs_{0.85}PbBr_3$.

annealing temperature increases, the average crystallite size reduces from 17.9 nm at 70 °C to 15.5 nm at 110 °C, with our findings aligning with other reports.[44,45] This reduction in the crystallite size indicates a densely packed microstructure with increased grain boundaries.

Fig. 7 presents a schematic illustration of the $FA_xCs_{1-x}PbBr_3$ crystal structure. During the standard fabrication method for $CsPbBr_3$ (without FA or PEABr), it has been demonstrated that Br^- vacancies occur due to the rapid nucleation rate,[46,47] resulting in poor morphology and traps,[48] which leads to very low emissions, as shown in Fig. S3–S6. Accordingly, the CsBr/PEABr doping scheme first introduces PEABr into the perovskite solutions, thereby filling the partial Br vacancies, which is favorable for the growth of high-quality films. Afterward, FA^+ was partially substituted, which can also lead to a significant increase in the Br-concentration and a slight increase in the lattice structure of the $FA_xCs_{1-x}PbBr_3$ framework,[49] as evident in the SEM and AFM images (Fig. 4b–f and 5b–f), thereby decreasing the defects and possibly enabling charge transport in the perovskite film.

XPS was used to track the surface composition. Table 1 summarizes the perovskite components in relative mole% with Pb^{2+} fixed at 1.0, similar to Maniyarasu *et al.*[50] When FA is incorporated into the perovskite lattice as FA^+, one of the two nitrogen atoms is charged and chemically shifted relative to the remaining nitrogen. The uncharged FA^+ nitrogen was observed at 400.3 ± 0.1 eV, while the charged one was shifted to 402.0 ± 0.2 eV. Nitrogen in PEA contains a single charged nitrogen atom, which is present at the same position (402.0 ± 0.2 eV). To quantify the data in Table 1, we assumed that only FA^+ were present in the perovskite lattice and that PEA was present at the surface layer. The uncharged N (400.3 eV) represented only FA^+, and since that molecule only contains one uncharged nitrogen, the atom% measured by XPS was effectively the mole% of that molecule in each sample.

In addition, as shown in Table 1, the mole% of PEA was determined by quantifying the non-FA charged nitrogen and then accounting for 8 carbon atoms associated with that molecule. The PEA did constitute a significant amount of the overall signal, consistent with it forming predominantly at the surface. Fig. 8 shows a progression of nitrogen 1s spectra containing increasing proportions of FA^+ relative to Cs^+ and PEA. There was generally good agreement between the expected surface composition and the measured composition by XPS for

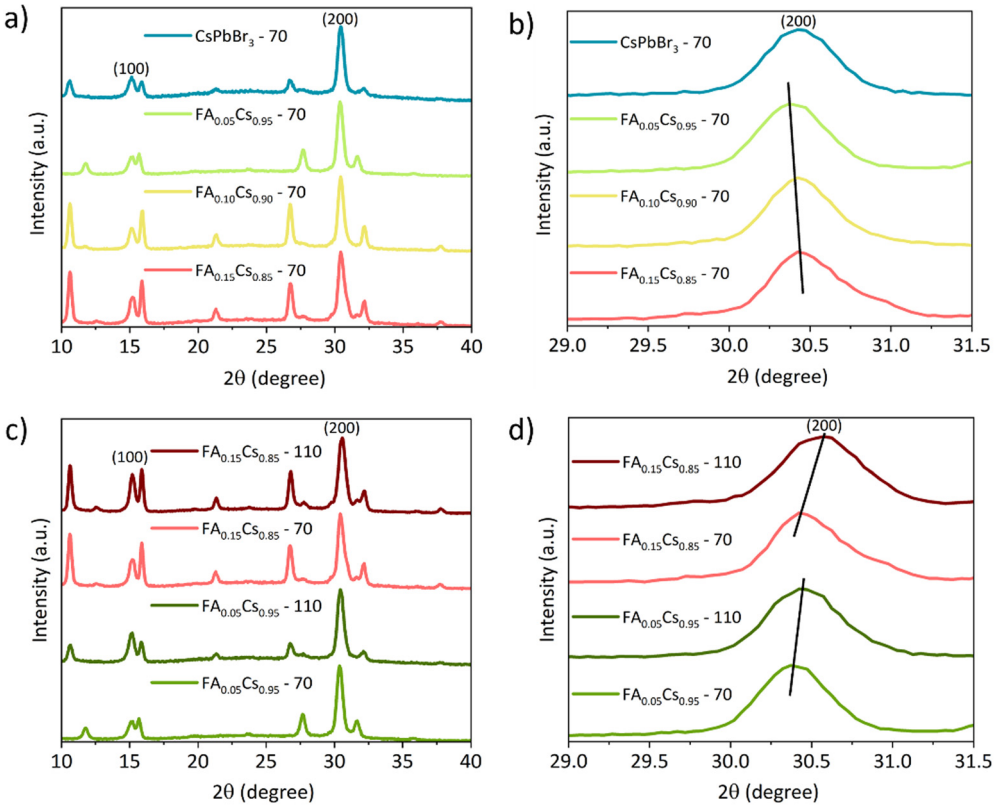

Fig. 6 XRD spectra of $FA_xCs_{1-x}PbBr_3$ ($0 < x < 0.15$) films annealed at (a) 70 °C and (b) their magnified (200) diffraction peak. Selected XRD spectra of $FA_xCs_{1-x}PbBr_3$ ($0 < x < 0.15$) thin films comparing films annealed at (c) 70 °C and 110 °C and (d) their magnified (200) diffraction peak.

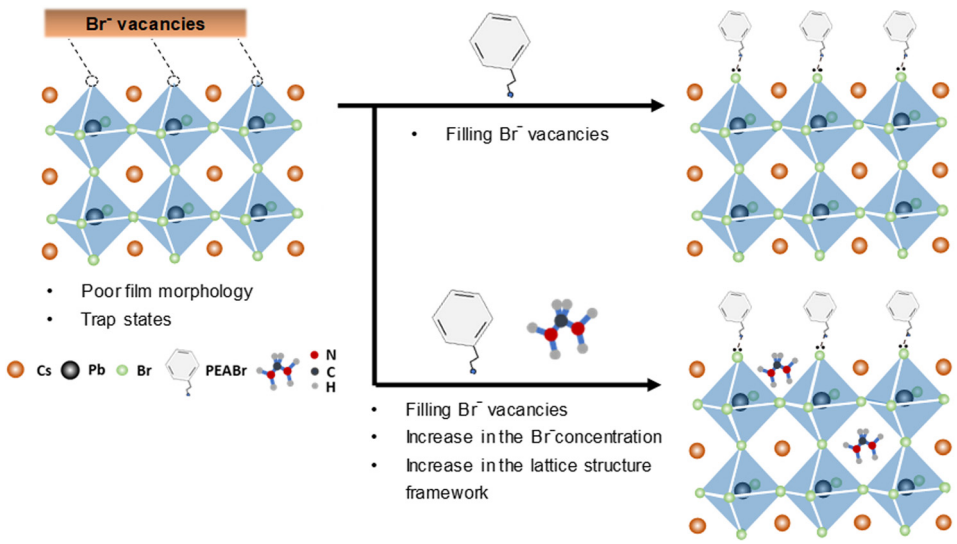

Fig. 7 Illustration of the mechanisms of additive-assisted strategy for PEABr and FA^+ incorporation in $CsPbBr_3$ perovskite films.

the 110 °C films. The 70 °C films all contained excess Cs^+ and Br^- ions, suggesting the possible presence of CsBr on the surfaces. Overall, we observed that the addition of an optimum amount of PEABr promotes the formation of compact perovskite films, and in this case, without significantly altering the optical properties, as evidenced by the SEM, XPS, UV-Vis, and PL measurements.

For the preliminary results of the fabricated light-emitting diodes, we employed a simple device architecture of ITO/PEDOT:PSS (poly(3,4-ethylenedioxythiophene)/perovskite)/LiF/

Table 1 Summary of XPS results in relative mole% (Pb^{2+} = 1.0)

	A-site		B-site	X-site	
Perovskite	Cs	$N–C^+$ (FA)	Pb	Br	PEA
Cs-70	1.5	—	1.0	2.3	—
Cs + PEABr-70	1.1	—	1.0	2.6	51.4
$FA_{0.05}Cs_{0.95}$-110	1.1	0.1	1.0	2.6	33.0
$FA_{0.05}Cs_{0.95}$-70	2.2	0.1	1.0	5.3	23.4
$FA_{0.10}Cs_{0.90}$-110	2.1	0.3	1.0	5.0	21.2
$FA_{0.10}Cs_{0.90}$-70	2.4	0.3	1.0	5.1	22.4
$FA_{0.15}Cs_{0.85}$-110	1.0	0.2	1.0	2.5	5.3
$FA_{0.15}Cs_{0.85}$-70	2.3	0.4	1.0	5.1	11.1

Al (Fig. 9a), without using traditional electron transport layers such as TPBi or F8BT, or employing Ba/Al or Ca/Al.[51–53] Fig. 9a shows the device architecture for the optimized film at 70 °C, while the *J–V* and luminance (*L–V*) characteristics are displayed in Fig. 9b and c, with the turn-on voltage varying between 2 V and 6 V. Moreover, as shown in Fig. 9c, the 510–512 nm PeLEDs exhibit peak luminance of 102, 225, 11, and 87 cd m^{-2}, respectively, for Cs, $FA_{0.05}Cs_{0.95}$, $FA_{0.10}Cs_{0.90}$, and $FA_{0.15}Cs_{0.85}$. All samples exhibit low EQE, with $FA_{0.05}Cs_{0.95}$ showing the highest value among the other ratios. The EL spectra are shown in Fig. 9d, with the device under operation (inset). We examined the spectra stability of the green $FA_{0.05}Cs_{0.95}$ LEDs by increasing the voltage from 0 V to 6 V (Fig. 9e). The EL peak remained stable at 511 ± 1 nm, and the full width at half maximum remained unchanged at 24.4 nm. All the devices exhibit a green EL emission, while $FA_{0.05}Cs_{0.95}$ LED corresponds to the Commission Internationale de L'Eclairage (CIE) color coordinates of (x = 0.076, y = 0.678) with color purity of 0.803, as shown in Fig. 9f. The summary of the perovskite materials and device structure for the green PeLEDs with the corresponding CIE coordinates compared to literature is shown in Table S4.

Although we observed that the quality of the film improves with the addition of PEABr and FA^+, the device performance is lower than usually reported in the literature.[54,55] The translation of improved film quality into device performance will require further work and improvement to reflect this observation in PeLEDs, as device architecture and other parameters may play a crucial role. However, these findings are promising and a good indication for PeLED device applications. Therefore, future research efforts may optimize the device structure and material properties in these perovskite thin films to achieve highly efficient and stable green light-emitting diodes.

Conclusions

In this study, we found that toluene outperforms anisole and chlorobenzene as an anti-solvent in the studied $CsPbBr_3$ and $FA_xCs_{1-x}PbBr_3$ perovskite films. More importantly, we found

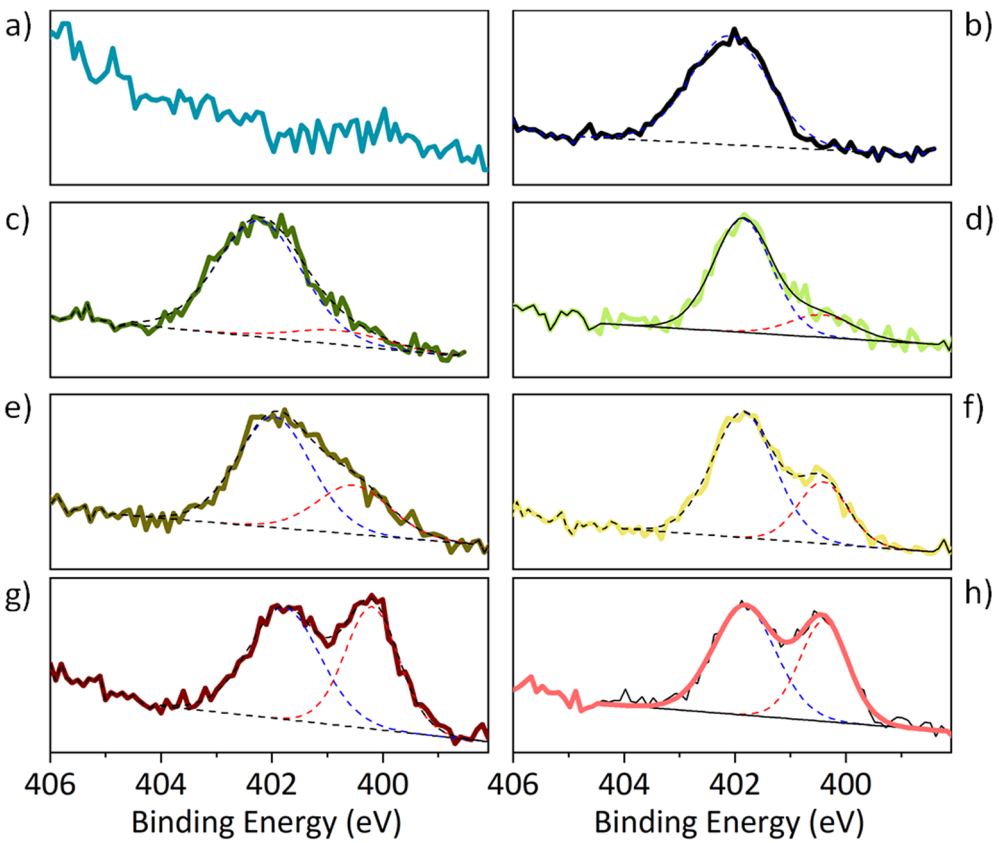

Fig. 8 Nitrogen 1s spectra curve fit into NH_2 (400.3 eV) and $C-NH_3^+$ (402.0 eV). (a) Cs-70, (b) PEA only, (c) $FA_{0.05}Cs_{0.95}$-110, (d) $FA_{0.05}Cs_{0.95}$-70, (e) $FA_{0.10}Cs_{0.90}$-110, (f) $FA_{0.10}Cs_{0.90}$-70, (g) $FA_{0.15}Cs_{0.85}$-110, (h) $FA_{0.15}Cs_{0.85}$-70.

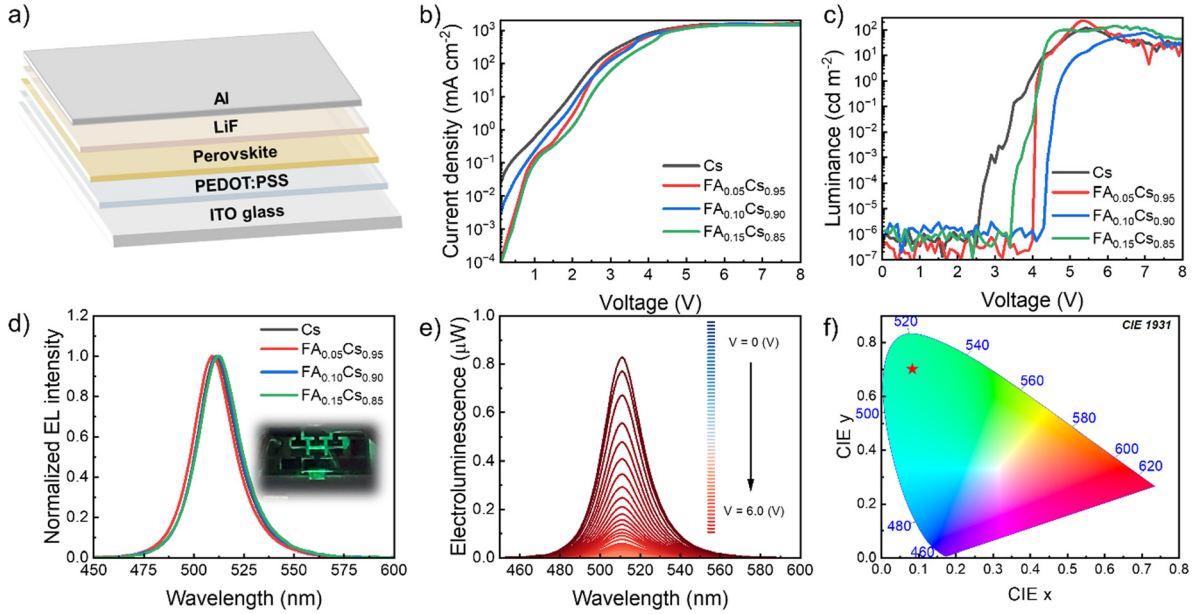

Fig. 9 Performance of fabricated Cs, $FA_{0.05}Cs_{0.95}$, $FA_{0.10}Cs_{0.90}$, and $FA_{0.15}Cs_{0.85}$ LEDs showing their (a) simple device architecture, (b) *J*–*V* curves, (c) luminance (*L*–*V*) curves, and (d) electroluminescence with device under operation (visual image of the device emitting green light, inset). (e) Electroluminescence at varying voltages and (f) the CIE color coordinates and the operating LED showing the green emission for $FA_{0.05}Cs_{0.95}$ LED.

that incorporating a small portion of FA^+ in Cs-based perovskite and adjusting the annealing temperature substantially impacts the optical, structural, morphological, and transport properties of the perovskite film. Our experiments demonstrated that an increase in the FA^+ ratio leads to a slight shift in the optical bandgap and the (200) XRD peaks toward higher wavelengths and 2θ angles, respectively, which becomes even more pronounced at a higher temperature, thus improving the crystallinity and formation of larger grain sizes. The chemical changes, large grain sizes, and defect and trap reduction can significantly promote effective charge transport within the perovskite thin film, as indicated by the preliminary device performance results. While our findings contribute valuable insights into studying antisolvent treatment and A-site cations modification in perovskite materials for thin films, future research should aim to optimize the FA/Cs ratio, device structure, and material properties, which are essential for achieving high-quality perovskite light-emitting diodes.

Experimental methods

Materials

Lead bromide ($PbBr_2$; 99.999%), cesium bromide (CsBr; 99.999%), dimethyl sulfoxide (DMSO; 99.9%), dimethylformamide (DMF; 99.9%), toluene (99.8%), anisole (99.8%) and chlorobenzene (CB; 99.8%) were purchased from Sigma Aldrich, and PEABr (99.9%) was purchased from Greatcell Solar Materials. The PEDOT:PSS (Clevios™ Al 4083) was purchased from Heraeus Epurio, and LiF was purchased from Kurt J Lesker Company. All materials were used as received.

Formulation of perovskite precursor solution and fabrication

We prepared a 0.3 M $CsPbBr_3$ precursor solution by dissolving the mixture of stoichiometric quantities of the $CsBr/PbBr_2$ in DMSO. An appropriate molar excess ratio of the 0.6 M PEABr was added to the 0.3 M $CsPbBr_3$ precursor solution. We prepared a 0.3 M $FA_xCs_{1-x}PbBr_3$ ($0 < x < 0.15$) precursor solution by dissolving the mixture of stoichiometric quantities of the $FABr/CsBr/PbBr_2$ in DMF/DMSO. Also, an appropriate molar excess ratio of the 0.6 M PEABr was added to the 0.3 M $FA_xCs_{1-x}PbBr_3$ ($0 < x < 0.15$) precursor solution. All precursor preparation was carried out in an N_2 glove box with an oxygen content of <10 ppm (parts per million). All ITO and glass substrates were sonicated with deionized water, acetone, and ethanol for 15 minutes. Before the perovskite deposition, all substrates were treated with ultraviolet ozone for 20 minutes. Based on the characterization study, all precursor solutions were spin-coated on a clean ITO or glass substrate at 5000 rpm for 60 s, respectively. Toluene was dropped onto the spinning ITO or glass substrate of $CsPbBr_3$ and $FA_xCs_{1-x}PbBr_3$ ($0 < x < 0.15$) films between 16 and 23 seconds. We annealed the $CsPbBr_3$ films at 70 °C for 10 minutes, while the $FA_xCs_{1-x}PbBr_3$ ($0 < x < 0.15$) films were annealed at 70 °C, 90 °C, and 110 °C, respectively.

Thin film characterization

To examine the morphological evolution of perovskite thin films, we employed field-emission scanning electron microscopy (FE-SEM) with a Verios G4 UC SEM (Thermo Scientific, Hillsboro, OR). The Bruker Dimension FastScan series was used for the AFM measurements. The measurements were carried out using a PerkinElmer LAMBDA 1050+ UV-vis-NIR spectrophotometer.

The photoluminescence (PL) and time-resolved PL spectra on glass/perovskite films were obtained using an FLS1000 photoluminescence spectrometer (Edinburgh Instrument, FLS1000). The PL excitation wavelength was 430 nm, and TRPL was enabled by a time-correlated single photon counting (TCSPC) diode. The decay curves were then fitted using OriginPro 2025 software to determine the lifetime constants. The XRD measurements were performed using a 240 mm radius Panalytical Empyrean® theta–theta X-ray diffractometer equipped with a copper (Cu) line source [Kα1–2 = 1.540598/1.544426 Å] X-ray tube. X-ray diffraction patterns were collected at 40 kV and 40 mA. Data were collected with a step size of 0.0501° from 10 to 50° 2-theta. The phase ID was performed using Jade® software (version 8.9) from Materials Data Inc. (MDI) and the International Centre for Diffraction Data (ICDD) PDF5® database.

A physical electronics VersaProbe III instrument equipped with a monochromatic Al kα X-ray source ($h\nu$ = 1486.6 eV) and a concentric hemispherical analyzer were used to perform XPS measurements. The samples were mounted in an argon glovebox with <1 ppm O_2 and transferred to the XPS system in a special inert sample transfer vessel to minimize air/moisture exposure. Charge neutralization was not utilized, and Oxygen was not observed on any surface. The binding energy axis was calibrated using sputter-cleaned Au foils (Au $4f_{7/2}$ = 83.96 eV) and Cu (Cu $2p_{3/2}$ = 932.62 eV, Cu $3p_{3/2}$ = 75.1 eV). A typical sampling depth of 3–6 nm (95% of the signal originated from this depth or shallower) was achieved when the measurement was done at a takeoff angle of 45° from the sample surface plane. Accounting for the X-ray cross section and inelastic mean free path of the electrons, quantification was made using instrumental relative sensitivity factors. The sample's analysed spot was ~200 μm in diameter. Minor elements show significantly higher standard deviations on homogeneous samples, and major elements (>5 atom%) yield standard deviations of < 3%.

Perovskite LED fabrication and characterization

Pre-patterned ITO substrates (1.1 × 25 × 25 mm, 12–20 Ω sq^{-1}, Colorado Concept Coating LLC) were sequentially sonicated with deionized water, acetone, and ethanol for 15 minutes. The substrates were then dried in the oven at 120 °C for 20 minutes. After cooling down, they were treated with ultraviolet ozone for 20 minutes before use. PEDOT:PSS (Clevios™ Al 4083) was spin-coated on the ITO substrates at 3000 rpm for 40 s, respectively, and then annealed at 120 °C for 10 minutes. The coated substrates were transferred to the glovebox (O_2 < 0.1 ppm and H_2O < 0.1 ppm) for perovskite layer deposition. All precursor solutions were spin-coated on the PEDOT:PSS layer at 5000 rpm for 60 s, respectively. Toluene was dropped on the spinning substrate of $FA_xCs_{1-x}PbBr_3$ ($0 < x < 0.15$) films between 16 and 23 s, after which the films were annealed at 70 °C for 10 minutes. LiF and Al layers were thermally evaporated on top of the perovskite films, with thicknesses of 2 and 100 nm, respectively. The device area was 0.15 cm^2. The performance of PeLEDs was measured in an N_2 glovebox using an ENLITECH LQ-50X-EL high speed/high sensitivity electroluminescence efficiency test system setup with a Keithley 2450 sourcemeter unit. The current density–voltage (J–V) curve was obtained by scanning the voltage from 0 to 9 V (forward scan) with a step of 0.1 V.

Author contributions

Ethan Jansen: data curation, investigation, methodology, formal analysis, validation, and writing – review; Ben York: data curation, investigation, formal analysis, validation, and writing – review; Souk Y. Kim: investigation, methodology, formal analysis, validation, visualization, writing – revised draft, and writing – review & editing; Jeffrey Shallenberger: data curation, formal analysis, methodology, validation, visualization, writing – original draft, and writing – review & editing; Ivy M. Asuo: conceptualization, investigation, resources, methodology, formal analysis, validation, visualization, writing – original draft, and writing – review & editing; Nutifafa Y. Doumon: conceptualization, data curation, formal analysis, investigation, methodology, project administration, supervision, funding acquisition, validation, visualization, writing – original draft, and writing – review & editing; and Kester O. Ighodalo: conceptualization, data curation, formal analysis, investigation, methodology, project administration, supervision, funding acquisition, validation, visualization, writing – original draft, and writing – review & editing.

Conflicts of interest

The authors declare no conflict of interest.

Data availability

The data supporting this article have been included as part of the SI.

Additional figures and data on the absorbance, atomic force microscopy (AFM) images, photoluminescence (PL), time-resolved PL (TRPL), fluorescence images of thin films under UV light, crystallite sizes, and a summary table of our device performance compared to other published studies. It also features a short video showcasing the operation of the PeLEDs device. See DOI: **https://doi.org/10.1039/d5tc01143d**

Acknowledgements

The authors acknowledge Penn State Materials Characterization Lab for the use of the Malvern Panalytical Empyrean III and field-emission scanning electron microscopy (FE-SEM) Verios G4 UC SEM (Thermo Scientific, Hillsboro, OR) and staff Nichole M. Wonderling and Julie M. Anderson for help with the XRD and SEM measurements. The authors would like to thank Oluwatosin S. Obaseki for his assistance with proofreading the first draft. KOI acknowledges the use of facilities and instrumentation supported by NSF through the Penn State Center for Nanoscale Science, Materials Research Science and Engineering Center [DMR-2011839]. KOI acknowledges the support from

the Office of the Dean of the Natural and Applied Sciences for funding this research. KOI acknowledges the Nyenhuis grant from the Brookstra Faculty Development Fund. EJ acknowledges the Doumon lab for the supervision, help, and discussion during his partial summer research time at Penn State, University Park. IMA acknowledges support from the Institute of Energy and the Environment (IEE) of The Pennsylvania State University, University Park. NYD acknowledges support from the Materials Research Institute (MRI) of The Pennsylvania State University, University Park.

References

1 Z. Liu, W. Qiu, X. Peng, G. Sun, X. Liu, D. Liu, Z. Li, F. He, C. Shen, Q. Gu, F. Ma, H.-L. Yip, L. Hou, Z. Qi and S.-J. Su, *Adv. Mater.*, 2021, **33**, 2103268.
2 W. Bai, T. Xuan, H. Zhao, H. Dong, X. Cheng, L. Wang and R.-J. Xie, *Adv. Mater.*, 2023, **35**, 2302283.
3 J. Jiang, Z. Chu, Z. Yin, J. Li, Y. Yang, J. Chen, J. Wu, J. You and X. Zhang, *Adv. Mater.*, 2022, **34**, 2204460.
4 B. Zhao, B. Guo, S. Xing, Z. Liu, Y. Yuan, Z. Ren, W. Tang, Y. Lian, G. Zhang, C. Zou and D. Di, *Matter*, 2024, **7**, 772–793.
5 K. H. Ngai, X. Sun, Y. Wang, L. Lin, Z. Chen, Q. Wei, M. Li, C. Luan, W. Zhang, J. Xu and M. Long, *Adv. Funct. Mater.*, 2023, **33**, 2211830.
6 Z. Xiao, Q. Wang, X. Wu, Y. Wu, J. Ren, Z. Xiong and X. Yang, *Org. Electron.*, 2020, **77**, 105546.
7 Y. Ma, Y. Wang, Y. Fang, Y. Jiang, Z. Dai and J. Miao, *Adv. Opt. Mater.*, 2024, **12**, 2401367.
8 K. O. Ighodalo, W. Chen, Z. Liang, Y. Shi, S. Chu, Y. Zhang, R. Khan, H. Zhou, X. Pan, J. Ye and Z. Xiao, *Angew. Chem., Int. Ed.*, 2023, **62**, e202213932.
9 Y. Shao, F. Dong, X. Zhu, J. Yang and Y. Sun, *ACS Appl. Electron. Mater.*, 2024, **6**, 6140–6146.
10 M. Abdi-Jalebi, Z. Andaji-Garmaroudi, S. Cacovich, C. Stavrakas, B. Philippe, J. M. Richter, M. Alsari, E. P. Booker, E. M. Hutter, A. J. Pearson, S. Lilliu, T. J. Savenije, H. Rensmo, G. Divitini, C. Ducati, R. H. Friend and S. D. Stranks, *Nature*, 2018, **555**, 497–501.
11 M. Saliba, T. Matsui, J.-Y. Seo, K. Domanski, J.-P. Correa-Baena, M. K. Nazeeruddin, S. M. Zakeeruddin, W. Tress, A. Abate, A. Hagfeldt and M. Grätzel, *Energy Environ. Sci.*, 2016, **9**, 1989–1997.
12 T. Sato, S. Takagi, S. Deledda, B. C. Hauback and S.-I. Orimo, *Sci. Rep.*, 2016, **6**, 23592.
13 B. Xu, W. Wang, X. Zhang, W. Cao, D. Wu, S. Liu, H. Dai, S. Chen, K. Wang and X. Sun, *J. Mater. Chem. C*, 2017, **5**, 6123–6128.
14 Z. Yuan, Z. Hu, I. Persson, C. Wang, X. Liu, C. Kuang, W. Xu, S. Bai and F. Gao, *Joule*, 2022, **6**, 2423–2436.
15 Q. Shan, J. Song, Y. Zou, J. Li, L. Xu, J. Xue, Y. Dong, B. Han, J. Chen and H. Zeng, *Small*, 2017, **13**, 1701770.
16 A. Senocrate, T. Acartürk, G. Y. Kim, R. Merkle, U. Starke, M. Grätzel and J. Maier, *J. Mater. Chem. A*, 2018, **6**, 10847–10855.
17 S. Premkumar, K. Kundu and S. Umapathy, *Nanoscale*, 2019, **11**, 10292–10305.
18 S. S. H. Dintakurti, P. Vashishtha, D. Giovanni, Y. Fang, N. Foo, Z. Shen, C. Guet, T. C. Sum and T. White, *RSC Adv.*, 2021, **11**, 24137–24143.
19 J. Si, Y. Liu, N. Wang, M. Xu, J. Li, H. He, J. Wang and Y. Jin, *Nano Res.*, 2017, **10**, 1329–1335.
20 Y.-H. Liu, R. K. Singh, S.-A. Lu, S. Som and C.-H. Lu, *J. Taiwan Inst. Chem. Eng.*, 2022, **139**, 104469.
21 H. Cho, J. S. Kim, C. Wolf, Y.-H. Kim, H. J. Yun, S.-H. Jeong, A. Sadhanala, V. Venugopalan, J. W. Choi, C.-L. Lee, R. H. Friend and T.-W. Lee, *ACS Nano*, 2018, **12**, 2883–2892.
22 K. Chen, S. Schünemann, S. Song and H. Tüysüz, *Chem. Soc. Rev.*, 2018, **47**, 7045–7077.
23 L. Zhang, X. Yang, Q. Jiang, P. Wang, Z. Yin, X. Zhang, H. Tan, Y. Yang, M. Wei, B. R. Sutherland, E. H. Sargent and J. You, *Nat. Commun.*, 2017, **8**, 15640.
24 Y. Shi, J. Xi, T. Lei, F. Yuan, J. Dai, C. Ran, H. Dong, B. Jiao, X. Hou and Z. Wu, *ACS Appl. Mater. Interfaces*, 2018, **10**, 9849–9857.
25 M. Jiang, X. Zhang and F. Wang, *Adv. Mater.*, 2024, **36**, 2400565.
26 L. Zhao, Y. Zhou, Z. Shi, Z. Ni, M. Wang, Y. Liu and J. Huang, *Nat. Photonics*, 2023, **17**, 315–323.
27 C. Wang, Y. Zhang, A. Wang, Q. Wang, H. Tang, W. Shen, Z. Li and Z. Deng, *Chem. Mater.*, 2017, **29**, 2157–2166.
28 J. Godet, G. Massé, I. Shahine, Q. Hatte, H. Bahsoun, F. Bouard, L. Vernisse, L. Pizzagalli, M. Le Granvalet and P.-Y. Tessier, *Thin Solid Films*, 2023, **787**, 140136.
29 A. D. Taylor, Q. Sun, K. P. Goetz, Q. An, T. Schramm, Y. Hofstetter, M. Litterst, F. Paulus and Y. Vaynzof, *Nat. Commun.*, 2021, **12**, 1878.
30 B. Zhou, P. Zhao, J. Guo, Y. Qiao, S. Hu, X. Guo, J. Liu and C. Li, *Nano Energy*, 2024, **124**, 109487.
31 I. M. Asuo, A. Mahdavi Varposhti, E. D. Gomez and N. Y. Doumon, *J. Mater. Chem. C*, 2024, **12**, 7562–7571.
32 I. M. Asuo, D. Gedamu, N. Y. Doumon, I. Ka, A. Pignolet, S. G. Cloutier and R. Nechache, *Mater. Adv.*, 2020, **1**, 1866–1876.
33 D. Gedamu, I. M. Asuo, D. Benetti, M. Basti, I. Ka, S. G. Cloutier, F. Rosei and R. Nechache, *Sci. Rep.*, 2018, **8**, 12885.
34 J. Jiang, M. Shi, Z. Xia, Y. Cheng, Z. Chu, W. Zhang, J. Li, Z. Yin, J. You and X. Zhang, *Sci. Adv.*, 2024, **10**, eadn5683.
35 J. C. Yu, J. H. Park, S. Y. Lee and M. H. Song, *Nanoscale*, 2019, **11**, 1505–1514.
36 M. Ban, Y. Zou, J. P. H. Rivett, Y. Yang, T. H. Thomas, Y. Tan, T. Song, X. Gao, D. Credgington, F. Deschler, H. Sirringhaus and B. Sun, *Nat. Commun.*, 2018, **9**, 3892.
37 M. R. Filip, G. E. Eperon, H. J. Snaith and F. Giustino, *Nat. Commun.*, 2014, **5**, 5757.
38 H. Zalrhi, M. Ouafi, M. Regragui, B. M. Soucase, F. Baig, Y. H. Khattak, U. Shafi, M. Abd-lefdil and L. Atourki, *RSC Adv.*, 2024, **14**, 15048–15057.
39 R. J. Stoddard, F. T. Eickemeyer, J. K. Katahara and H. W. Hillhouse, *J. Phys. Chem. Lett.*, 2017, **8**, 3289–3298.

40 Y. Guo, S. Apergi, N. Li, M. Chen, C. Yin, Z. Yuan, F. Gao, F. Xie, G. Brocks, S. Tao and N. Zhao, *Nat. Commun.*, 2021, **12**, 644.
41 X. Yu, J. Guo, Y. Mao, C. Shan, F. Tian, B. Meng, Z. Wang, T. Zhang, A. K. K. Kyaw, S. Chen, X. Sun, K. Wang, R. Chen and G. Xing, *Nano-Micro Lett.*, 2024, **16**, 205.
42 S. Wang, S. Frisch, H. Zhang, O. Yildiz, M. Mandal, N. Ugur, B. Jeong, C. Ramanan, D. Andrienko, H. I. Wang, M. Bonn, P. W. M. Blom, M. Kivala, W. Pisula and T. Marszalek, *Mater. Horiz.*, 2022, **9**, 2633–2643.
43 P. Cottingham and R. L. Brutchey, *Chem. Commun.*, 2016, **52**, 5246–5249.
44 L. K. Singh, A. Bhadauria, S. Jana and T. Laha, *Acta Metall. Sin. (Engl. Lett.)*, 2018, **31**, 1019–1030.
45 K.-C. Yeh and C.-H. Chan, *Sci. Rep.*, 2024, **14**, 3351.
46 K. Shen, H. Xu, X. Li, J. Guo, S. Sathasivam, M. Wang, A. Ren, K. L. Choy, I. P. Parkin, Z. Guo and J. Wu, *Adv. Mater.*, 2020, **32**, 2000004.
47 Y. Wu, C. Wei, X. Li, Y. Li, S. Qiu, W. Shen, B. Cai, Z. Sun, D. Yang, Z. Deng and H. Zeng, *ACS Energy Lett.*, 2018, **3**, 2030–2037.
48 I. du Fossé, J. T. Mulder, G. Almeida, A. G. M. Spruit, I. Infante, F. C. Grozema and A. J. Houtepen, *J. Am. Chem. Soc.*, 2022, **144**, 11059–11063.
49 Y. R. Park, S. Eom, H. H. Kim, W. K. Choi and Y. Kang, *Sci. Rep.*, 2020, **10**, 14758.
50 S. Maniyarasu, B. F. Spencer, H. Mo, A. S. Walton, A. G. Thomas and W. R. Flavell, *J. Mater. Chem. A*, 2022, **10**, 18206–18217.
51 D. Ye, Z. Li, W. Chen, K. O. Ighodalo, P. Xiao, T. Chen and Z. Xiao, *ACS Appl. Mater. Interfaces*, 2022, **14**, 34918–34925.
52 D. Abbaszadeh, G. A. H. Wetzelaer, N. Y. Doumon and P. W. M. Blom, *J. Appl. Phys.*, 2016, **119**, 095503.
53 D. Abbaszadeh, N. Y. Doumon, G.-J. A. H. Wetzelaer, L. J. A. Koster and P. W. M. Blom, *Synth. Met.*, 2016, **215**, 64–67.
54 L. Kong, Y. Luo, Q. Wu, X. Xiao, Y. Wang, G. Chen, J. Zhang, K. Wang, W. C. H. Choy, Y.-B. Zhao, H. Li, T. Chiba, J. Kido and X. Yang, *Light: Sci. Appl.*, 2024, **13**, 138.
55 J.-M. Hao, Z.-Y. Ma, Y.-H. Song, Y.-L. Hu, G.-J. Ding, S. U. Rahman, Y.-C. Yin, B.-S. Zhu, C.-M. Wang, Z. Zhao, M. Ge and H.-B. Yao, *Adv. Opt. Mater.*, 2025, e01235.